Dalton Transactions

ROYAL SOCIETY OF CHEMISTRY

PAPER

View Article Online
View Journal | View Issue

Cite this: *Dalton Trans.*, 2021, **50**, 16030

Polyoxoniobates as molecular building blocks in thin films†

Mark A. Rambaran, András Gorzsás, Michael Holmboe and C. André Ohlin *

Received 14th September 2021,
Accepted 30th September 2021

DOI: 10.1039/d1dt03116c

rsc.li/dalton

Niobium oxide thin films have been prepared by spin-coating aqueous solutions of tetramethylammonium salts of the isostructural polyoxometalate clusters $[Nb_{10}O_{28}]^{6-}$, $[TiNb_9O_{28}]^{7-}$ and $[Ti_2Nb_8O_{28}]^{8-}$ onto silicon wafers, and annealing them. The $[Nb_{10}O_{28}]^{6-}$ cluster yields films of Nb_2O_5 in the orthorhombic and monoclinic crystal phases when annealed at 800 °C and 1000 °C, respectively, whereas the $[TiNb_9O_{28}]^{7-}$ and $[Ti_2Nb_8O_{28}]^{8-}$ clusters yield the monoclinic crystal phases of $Ti_2Nb_{12}O_{29}$ and $TiNb_2O_7$ (titanium–niobium oxides) in different ratios. We also demonstrate a protocol for depositing successive layers of metal oxide films. Finally, we explore factors affecting the roughness of the films.

Introduction

To sustain the fast-paced energy- and technologically driven society we live in, we need to develop new materials, and improve on those currently in use. Many electronic devices, from mobile phones to MRI machines, rely on niobium pentoxide (Nb_2O_5) and tantalum pentoxide (Ta_2O_5).[1] The inertness of niobium and tantalum oxides is associated with good biocompatibility and corrosion resistance.[2,3] Important applications where niobium, tantalum and Nb/Ta-titanium oxide films are used include orthopaedic/orthodontic devices,[4,5] waveguides,[6] electromagnetic interference shielding,[7] and coatings for corrosion protection and biomedical devices.[8–11] Due to the extensive use of these metal oxides and a lack of alternatives, niobium and tantalum are classified as *technologically critical elements.*

Key challenges lie in sourcing – leading to coltan, the mineral mined to produce niobium and tantalum, being termed a 'blood mineral'[12] – and implementing sustainable recycling protocols due to the inertness of niobium and tantalum oxides. Hence, better atom economy in usage, coupled with improved recovery methods, are needed.

There is also a need to develop lead-free piezoelectric materials to circumvent the use of lead zirconium titanate (PZT) piezoelectric devices. Sodium potassium niobate (KNN) and lithium niobate ($LiNbO_3$) are considered suitable alternatives to PZT.[13] However, the methods of synthesising KNN thin films may be energy intensive, or lack reproducibility and require the use of toxic precursors,[14] and the ability to vary the alkali–metal content and type is very limited, which is of relevance to this study.

Translating recent advances in the understanding of polyoxoniobate and -tantalate chemistry[15] into novel methods for making thin films therefore promises to allow better control over the composition of the films, better atom economy, and access to films with improved or novel properties.

Polyoxoniobates and -tantalates are examples of polyoxometalates (POMs),[16–18] discrete anionic oxide clusters of group 5 and 6 metals in their highest oxidation states, and they are attractive as potential building blocks in the preparation of extended materials, such as thin films. In particular, the discrete nature of POMs means that their structures can be known with confidence, and their structures and composition can in many cases be tuned by targeted synthetic modifications.[15,19–25] At a minimum, this means that the elemental composition of the film can be controlled to a high degree, with the added possibility of the POM structure being wholly or partially retained in the solid film, so that the relative locations of individual atoms can be controlled.

Many POMs are also highly soluble – the solubility of tetramethylammonium ($[N(CH_3)_4]^+$; **TMA**) salts of the polyoxoniobates typically exceeds 1 g ml^{-1} in water, and are moderately soluble in methanol and ethanol, making them easy to handle and manipulate in the lab. Recently developed protocols for microwave synthesis offer short reaction times (15 to 60 minutes),[26] capable of yielding tens of grams of pure product in one-pot reactions in the lab. In addition, organic counter ions, such as TMA, can be removed by thermal decomposition,[27,28] something which is not possible with alkali ions. This allows for the production of films that can be

---

Department of Chemistry, Faculty of Science and Technology, Umeå University, 907 36 Sweden. E-mail: andre.ohlin@umu.se

† Electronic supplementary information (ESI) available: Details related to synthesis and film deposition, Raman, PXRD, ellipsometry, ^{17}O-NMR, EDS, SEM and AFM measurements. See DOI: 10.1039/d1dt03116c

freely doped with different ions and at different ratios. Finally, while there is a range of existing methods for making metal oxide films,[29–32] not all scale well, or can be applied to a wide range of substrates. Sol–gel,[29] sputter deposition[30] or laser ablation methods[31,32] may suffer from issues of reproducibility and/or cost.[32] The use of polyoxometalates circumvent these limitations, while offering the possibility of heteroatom doped Nb_2O_5 or Ta_2O_5 to be fabricated through soft methods. Film preparation through spin-coating of benign, non-volatile, water-compatible precursors that can easily be made in bulk quantities, is thus a very appealing idea.

Anhydrous niobium pentoxide (Nb_2O_5) – the most common form of niobium oxide – exhibits temperature-dependent polymorphism and can be made from amorphous hydrous Nb_2O_5 (or niobic acid). Pseudohexagonal TT-Nb_2O_5 forms between 500–600 °C, orthorhombic *ortho*-Nb_2O_5 (or T-Nb_2O_5) is obtained at 600 °C–800 °C, tetragonal M-Nb_2O_5 forms at 850 °C–950 °C, and monoclinic mono-Nb_2O_5 (or H-Nb_2O_5) is seen at >950 °C.[33–35] *ortho*- and mono-Nb_2O_5 prevail in the literature, with TT- and M-Nb_2O_5 being considered as metastable forms.[33–35]

Anhydrous Ta_2O_5 also exhibits polymorphism. It exists in an orthorhombic crystal system as L-Ta_2O_5 or *ortho*-Ta_2O_5 (low temperature form) below 1360 °C and reversibly converts to the H-Ta_2O_5 phase (high temperature form) above 1360 °C.[36–38] Other Ta_2O_5 polymorphs are accessible but require high pressures to promote their formation.[39] As with niobium, there exists a hydrated amorphous form, tantalic acid. The reactivity of these amorphous oxides is much higher than that of their anhydrous counterparts,[26] and have been demonstrated to be good precursors in polyoxoniobate and polyoxotantalate synthesis.[15,22–24,40]

Titanium–niobium oxides are also found as orthorhombic and monoclinic crystal systems. Crystalline $Ti_2Nb_{10}O_{29}$ is dimorphic and exists in both the orthorhombic and monoclinic crystal systems,[41] while the crystalline $TiNb_2O_7$ exists only in the monoclinic crystal system.[42] Both can be made from hydrous Nb_2O_5 (niobic acid) and TiO_2 directly at ≥1000 °C,[41–44] niobium citrate and $Ti(^iPrO)_4$,[45] or $NbCl_5$ and $Ti(^iPrO)_4$ as sources of hydrous Nb_2O_5 and TiO_2, respectively,[46,47] These methods are limited due to the extensive heating time and temperature required to form the titanium–niobium oxides from solid Nb_2O_5 and TiO_2. Notably, the titanium–niobium oxides are considered as prospective anode materials for lithium-ion batteries, to replace graphite or $Li_4Ti_5O_{12}$ anodes currently used.[48,49] Studies of the electrochemical properties of $Ti_2Nb_{10}O_{29}$ have determined it has a high rate capability and diffusion coefficient, which facilitates Li^+ and electron transport.[47,50,51] The $TiNb_2O_7$ is of particular interest because of its energy density and lithiation properties.[48]

Decaniobate (**Nb_{10}**) has been used as an aqueous precursor for depositing Nb_2O_5 and Nb_2O_5-ITO thin films on glass to elicit optical, electrochromic and electrochemical properties.[52–54] These studies were limited to temperatures below 400 °C in the annealing process of Nb_2O_5 due the thermal properties of ITO. Chemical condensation of Nb_2O_5 using formic acid was also investigated at room temperature.[54]

A comparative study by Fullmer *et al.*[27] of the Nb_2O_5 and Ta_2O_5 thin films deposited from aqueous solutions of hexaniobate (**Nb_6**) and hexatantalate (**Ta_6**), respectively, found that smooth Ta_2O_5 films always formed from Ta_6 – regardless of annealing temperature – unlike that of the Nb_2O_5 film from Nb_6. There was, in particular, a noticeable increase in the roughness of the Nb_2O_5 films formed at 600 °C and 800 °C, when compared to Ta_2O_5 films. This was attributed to a preference of either a lower activation energy of grain growth in Nb_2O_5, or the formation of proton-bridged Ta_6 dimers *vs.* linear proton-bridged Nb_6 chain-oligomers, with the latter serving as nucleation seeds.[27]

Mansergh *et al.*[28] further probed the orthorhombic Ta_2O_5 thin films deposited from Ta_6. Film thickness was determined to be directly proportional to the concentration of Ta_6, while film thickness decreased at elevated temperatures. The latter decrease is associated with the removal of water, and decomposition of the TMA as the film condenses. The Ta_2O_5 films also become courser following heating above 700 °C due to grain growth, which coincides with a decrease in the refractive index of the film above 600 °C.[28] More recently, Saez Cabezas *et al.*[55] have developed an electrochemical method for acid-catalyzed condensation of Nb_2O_5 and Ta_2O_5 thin films, from Nb_6 and Ta_6, respectively, *via* the potentiostatic oxidation of water. They determined both Nb_2O_5 and Ta_2O_5 film thickness to increase with the applied potential and that film thickness increases rapidly during the first two minutes of the electrochemical deposition process, after which it plateaus. Finally, Fast *et al.*[14] spin-coated multiple layers of potassium sodium niobate thin films from sodium/potassium hexaniobate, yielding homogeneous films. Hexaniobate is only stable at alkaline pH above 9–10, which limits the chemical compatibility with potential dopants. In addition, the use of alkali salts leads to the forced inclusion of alkali cations in the finished film, whether desirable or not.

In this study, we used solution deposition of polyoxoniobates to develop surfaces where the crystallinity, thickness and roughness can be tuned by changing the starting material, concentration, and annealing temperature. A multi-step protocol has been developed to ensure layered metal oxide thin films can be deposited through an iterative spin-coating and annealing process.

Experimental

Chemicals were used as received. $[NC(H_3)_4]_6[Nb_{10}O_{28}]\cdot 2H_2O$ (**Nb_{10}**), $[NC(H_3)_4]_7[TiNb_9O_{28}]\cdot 3H_2O$ (**$TiNb_9$**), $[NC(H_3)_4]_8[Ti_2Nb_8O_{28}]\cdot 6H_2O$ (**Ti_2Nb_8**), $[NC(H_3)_4]_8[Nb_6O_{19}]\cdot 2H_2O$ (**Nb_6**) and $[NC(H_3)_4]_8[Ta_6O_{19}]$ (**Ta_6**) were synthesised using microwave irradiation according to published procedures.[26,56] Aqueous solutions (0.2 M) of Nb_{10}, $TiNb_9$, Ti_2Nb_8, Nb_6 and Ta_6 were spin-coated onto silicon wafers (50 × 50 mm, p-type, 10–20 Ω cm, Siegert Wafer GmbH, Germany) pre-treated with piranha solution and atmospheric-pressure plasma. See ESI† for details. In the typical experiment, 100 μl of polyoxometalate solution (0.2 M) was placed at the centre of the substrate, and spun at 2000 rpm for four minutes, before annealing in a furnace using a ramped temperature program (see ESI† for details). Raman spectra of bulk solutions of polyoxoniobates and of annealed powders were collected using a 532 nm laser on an Anton-Paar Cora 5600 spectrometer. Raman spectra of spin-deposited films were collected using a Renishaw Qontor Raman microscope, using a 405 nm laser. Powder X-ray diffraction measurements were done on a PANalytical X'Pert^3 diffractometer with a CuK$_{\bar{\alpha}}$ source. Ellipsometry measurements were done using an Alpha-SE Ellipsometer (J.A. Woollam Co. Inc.). Atomic force microscopy imaging was done with a Bruker BioScope Catalyst instrument operating in peak force mode in air. See ESI† for additional details.

Results and discussion

We have explored the spin-coating of tetramethylammonium (TMA) salts of a series of polyoxoniobate and polyoxotantalate clusters – Nb_6, Nb_{10}, $TiNb_9$, Ti_2Nb_8 and Ta_6 (Fig. 1). These targets were chosen as the structures are known with great confidence, and their solution phase chemistries have been studied extensively.[57–60] While Ta_6 and Nb_6 are stable at pH 9, Nb_{10} is only stable in a very narrow pH region, *ca.* 5–7.5,[57] above which it dissociates to Nb_6. The replacement of one niobium atom by a titanium atom in Nb_{10}, however, extends this stability range to pH 6.5–12.0 in $TiNb_9$,[59] and for Ti_2Nb_8 no dissociation or speciation is evident even at pH 12.5.[60] While the microwave syntheses of Nb_{10}, Nb_6, Ta_6 and $TiNb_9$ have been reported,[26,56] for this work we also developed the microwave synthesis of Ti_2Nb_8. Although these molecules can be made through hydrothermal methods by heating overnight,[15,23,40] microwave synthesis affords these clusters after irradiation for 30 minutes, and can easily be scaled up to yield 10–15 grammes per one-pot batch. Rapid production of large quantities of compound is an important factor in making these types of clusters in industrial thin film synthesis both attractive and viable.

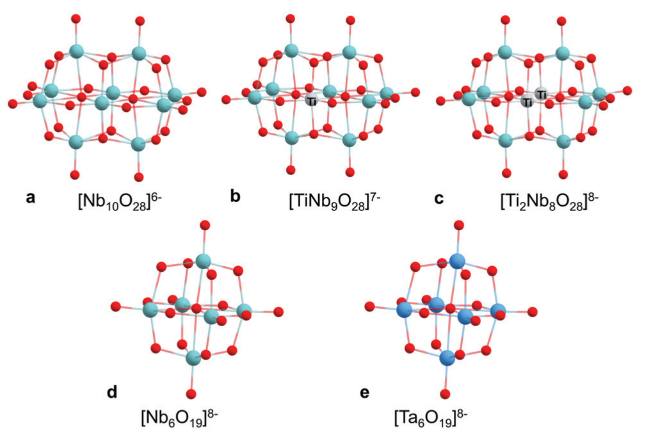

Fig. 1 The $[Nb_{10}O_{28}]^{6-}$ (a), $[TiNb_9O_{28}]^{7-}$ (b), $[Ti_2Nb_8O_{28}]^{8-}$ (c), $[Nb_6O_{19}]^{8-}$ (d) and $[Ta_6O_{19}]^{8-}$ (e) polyoxometalate ions. Red, light blue, grey and dark blue spheres represent oxygen, niobium, titanium and tantalum atoms, respectively.

Silicon wafers were chosen as the substrate in spin-coating deposition experiments as they have high smoothness, good chemical inertness, and can tolerate the elevated temperatures needed for annealing. Silicon substrates were cleaned with piranha solution – a 3 : 1 solution of concentrated sulfuric acid and 30% hydrogen peroxide – before being treated with atmospheric pressure plasma in a plasma chamber. This plasma treatment was necessary for the spin-coated polyoxometalates to adhere to the surface of the substrate.

First, the effects of the annealing temperature and polyoxometalate concentration were investigated. Based on spectroscopic ellipsometry, there is a consistent decrease in film thickness with increased annealing temperature up to 800 °C. The most notable change in thickness, however, occurs when the films are heated between 200 °C–400 °C and corresponds to removal of water and decomposition of the TMA counter ion. As expected, the film thickness increases at higher polyoxometalate concentrations. This is illustrated for the Nb_{10} and Ta_6 films in Fig. 2. At high polyoxometalate concentrations (0.5 M), the films are prone to spontaneous crystallisation after spin-coating and prior to annealing, leading to the formation of a transparent crystalline layer on the surface of the film. After annealing, this crystallisation is manifested in the presence of grain boundaries – especially at higher temperatures – that induce film coarseness and total internal reflection of incident light. The latter phenomenon limits the reproducibility of thickness measurements. Hence, 0.2 M polyoxometalate solutions were used throughout the study as this concentration yielded sufficiently thick films that could still be probed *via* spectroscopic ellipsometry.

Knowing that a phase change in Nb_2O_5 occurs between 800 °C and 1000 °C, we spin-coated aqueous solutions (0.2 M) of all polyoxometalates (Nb_{10}, $TiNb_9$, Ti_2Nb_8, Nb_6 and Ta_6) in water onto silicon wafers, and annealed the films at 800 or 1000 °C in air. Thereafter, the films were characterised by Raman spectroscopy, SEM and AFM.

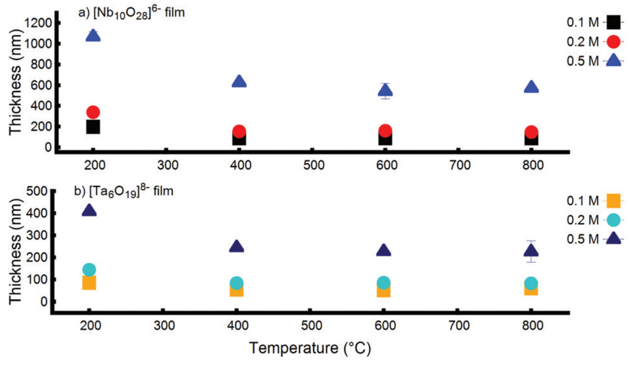

Fig. 2 Thickness of Nb_2O_5 (a) and Ta_2O_5 (b) films obtained from annealing Nb_{10} and Ta_6, respectively, and determined by ellipsometry.

Raman spectra of Nb_{10} films showed that mainly *ortho*-Nb_2O_5 is obtained after annealing at 800 °C, as indicated by the broad peak at *ca.* 690 cm^{-1} (Fig. 3a). Annealing at 1000 °C, similarly yielded mono-Nb_2O_5 as indicated by the Nb═O stretch at *ca.* 993 cm^{-1}. The crystal form of the film can thus be tuned by the choice of annealing temperature.

Powders of pure Nb_{10} were also annealed, to see whether this yielded the same products as annealed films. The Raman spectra of annealed powders showed the same behaviour as the thin films, with *ortho*- and mono-Nb_2O_5 dominating at 800 and 1000 °C, respectively (Fig. 3b). There is no evidence of residual TMA counter ion in either powder or film, indicating that it has been fully combusted during annealing. Powder XRD further confirmed the assignment of the crystal phases at 800 and 1000 °C, as well as showing that powders annealed at 200 and 400 °C remained amorphous (Fig. 3c). This agrees with previous results that determined amorphous Nb_2O_5 crystallisation commences at temperatures >400 °C.[61] Fig. 3d depicts the difference in packing of NbO_6 octahedra within Nb_2O_5 crystal lattice of *ortho*- and mono-Nb_2O_5. Films of Nb_6 behaved broadly the same as films of Nb_{10}, yielding *ortho*-Nb_2O_5 and mono-Nb_2O_5 at 800 °C and 1000 °C, respectively (Fig. S2-2†).

Raman spectra of films of $TiNb_9$ annealed at 800 and 1000 °C looked very similar to those obtained from Nb_{10}. However, a narrow band at *ca.* 997 cm^{-1} was observed at both temperatures (Fig. 4a). The thin film spectra were the same as those obtained from annealed $TiNb_9$ powder (Fig. 4b), which allowed us to determine the composition of the film using PXRD to be *ca.* 80% 1 : 1 orthorhombic and monoclinic $Ti_2Nb_{12}O_{29}$ (Fig. 4c), as well as 20% 1 : 1 orthorhombic and monoclinic Nb_2O_5, at both 800 °C and 1000 °C. The source of the Nb_2O_5 is two-fold: the titanium : niobium (Ti : Nb) ratio in $Ti_2Nb_{12}O_{29}$ is higher than in the starting material, and Nb_6 is present as a minor impurity in the one-pot synthesis of $TiNb_9$ (Fig. S7-4†). The peak at *ca.* 997 cm^{-1} in the Raman spectrum was assigned to Nb═O symmetric stretching and the broad band in the 600 cm^{-1} region is shifted in $Ti_2Nb_{12}O_{29}$ relative to Nb_2O_5, owing to the substitution of some of the NbO_6 octahedra by TiO_6 (Fig. 4d).

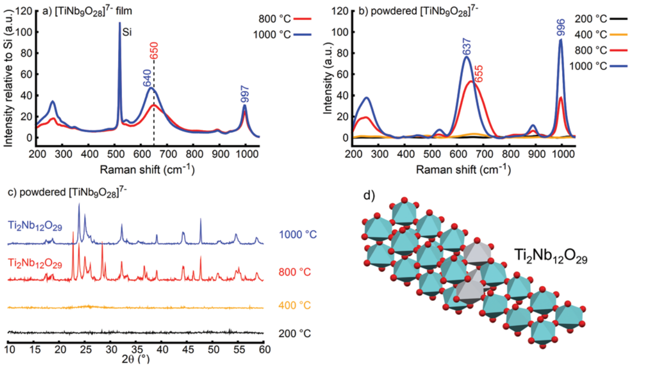

Fig. 4 (a) Raman spectra of $[TiNb_9O_{28}]^{7-}$ films annealed at 800 °C and 1000 °C, (b) Raman spectra and (c) PXRD patterns of powdered $[TiNb_9O_{28}]^{7-}$ annealed at selected temperatures and (d) the monoclinic $Ti_2Nb_{12}O_{29}$ titanium–niobium oxide. Red spheres represent oxygen atoms, light blue and grey octahedra represent niobium and titanium atoms, respectively. See ESI (Fig. S2-5†) for Raman signals of powdered $[TiNb_9O_{28}]^{7-}$ annealed at 200–400 °C.

Films of Ti_2Nb_8 annealed at 800 °C and 1000 °C also exhibited Raman spectra that were consistent with the spectra of annealed of Ti_2Nb_8 powders at the same temperatures (Fig. 5a and b). The Raman peak at *ca.* 1000 cm^{-1} is symptomatic of Nb═O symmetric stretching in $TiNb_2O_7$ and is consistent with the monoclinic crystal system. Raman peaks at *ca.* 646 cm^{-1} and 543 cm^{-1} are similarly attributable to stretches of NbO_6 octahedra and Nb–O–Nb bonds, respectively. PXRD confirmed the presence of monoclinic $TiNb_2O_7$ at 800 °C and 1000 °C (Fig. 5c). However, Rietveld refinement showed that the monoclinic $TiNb_2O_7$ obtained after annealing at 800 °C contained

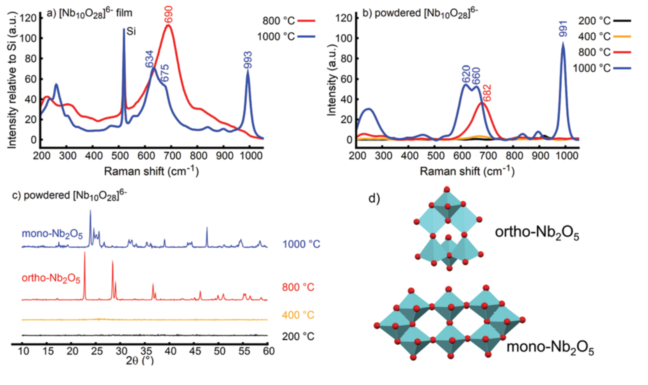

Fig. 3 (a) Raman spectra of $[Nb_{10}O_{28}]^{6-}$ films annealed at 800 °C and 1000 °C, (b) Raman spectra and (c) PXRD patterns of powdered $[Nb_{10}O_{28}]^{6-}$ annealed at 200–1000 °C and (d) *ortho*-Nb_2O_5 and mono-Nb_2O_5 polymorphs of Nb_2O_5. Red spheres represent oxygen atoms and light blue polyhedra niobium atoms. See ESI (Fig. S2-5†) for Raman signals of powdered $[Nb_{10}O_{28}]^{6-}$ annealed at 200–400 °C.

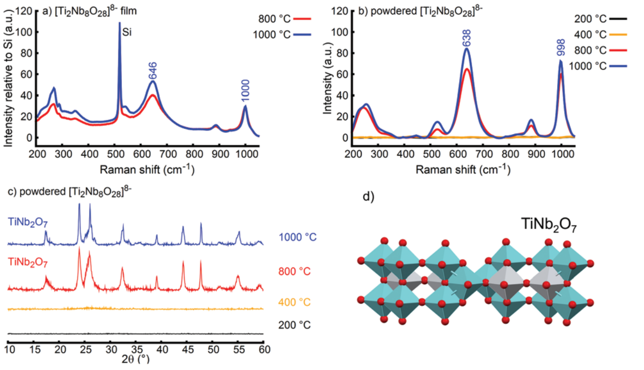

Fig. 5 (a) Raman spectra of $[Ti_2Nb_8O_{28}]^{8-}$ films annealed at 800 °C and 1000 °C, (b) Raman spectra and (c) PXRD patterns of powdered $[Ti_2Nb_8O_{28}]^{8-}$ annealed at selected temperatures and (d) the monoclinic $TiNb_2O_7$ titanium–niobium oxide. Red spheres represent oxygen atoms, light blue and grey octahedra represent niobium and titanium atoms, respectively. See ESI (Fig. S2-5†) for Raman signals of powdered $[Ti_2Nb_8O_{28}]^{8-}$ annealed at 200–400 °C.

ca. 16% 1 : 1 orthorhombic and monoclinic $Ti_2Nb_{12}O_{29}$, while *ca.* 34% 1 : 1 orthorhombic and monoclinic $Ti_2Nb_{12}O_{29}$ were present after annealing at 1000 °C. The $Ti_2Nb_{12}O_{29}$ likely stems from thermal decomposition of Ti_2Nb_8 during the annealing process and the Ti : Nb ratio of $TiNb_2O_7$ is higher than the starting material. Decomposition of Ti_2Nb_8 was confirmed by the observation that treatment of an aqueous solution of Ti_2Nb_8 at 160 °C for one hour yielded signals in the ^{17}O NMR spectrum that corresponded to a very low concentration of $TiNb_9$ (Fig. S7-5†). Notably, the shifting of the NbO_6 octahedra stretching to higher frequencies is similarly attributable to the presence of TiO_6 octahedra (substituting for NbO_6 octahedra) within the $TiNb_2O_7$ crystal lattice (Fig. 5d); much like $Ti_2Nb_{12}O_{29}$.

In contrast, annealing spin-coated films of Ta_6 did not yield films with Raman spectra that agreed with their annealed powder counterparts, mainly because Ta_6 films annealed at 800 °C and 1000 °C were Raman silent (Fig. 6a; only the background signal from the silicon wafer is observed). The Raman spectrum of powder obtained from annealed Ta_6 at 800 °C and 1000 °C showed that it consisted of *ortho*-Ta_2O_5 (Fig. 6b), an assignment which was confirmed by PXRD (Fig. 6c). The broad peak at 895 cm^{-1} originates from the stretching of Ta–O bonds with different bond strengths due to corner/edge-sharing in tantalum oxide polyhedra. *ortho*-Ta_2O_5 exhibits a Raman peak at 845 cm^{-1} that is attributable to Ta–O stretching of TaO_6 and TaO_7 (pentagonal bipyramidal) polyhedra. The Raman peaks at 620 cm^{-1} and 700 cm^{-1} are from stretches of TaO_6 octahedra, with the stretching at 700 cm^{-1} arising from Ta–O bonds with different bond strengths due to corner/edge-sharing polyhedra. The structure of crystalline *ortho*-Ta_2O_5 (Fig. 6d) depicts the different TaO_6 and TaO_7 polyhedra present in the crystal lattice.

The lack of a Raman signal from the Ta_6 films was attributed to attenuation specific to the tantalum oxide films. This was confirmed by depositing films of solutions of 1 : 1 Nb_6 : Ta_6, which yielded strongly attenuated spectra relative to pure Nb_6, whereas powders of the same solution showed no such attenuation (Fig. S2-6†).

Decomposition of the TMA counter ion in the annealed films was probed through energy-dispersive X-ray spectroscopy (EDS) (Fig. 7). The elemental composition of C after annealing at 400 °C decreases below 10%, and did not exceed 1% after annealing at 800–1000 °C. This correlates to rapid decomposition of the TMA counter ion at 200–400 °C and the continued decomposition of any carbon residues (char) at higher temperatures. There is a notable increase in the metal (Nb, Ti or Ta) composition of the annealed films at 200–400 °C, in agreement with decomposition of TMA, which later plateaus at 800–1000 °C.

The Ti content of annealed Ti_2Nb_8 films is higher than the Ti composition of annealed $TiNb_9$, which corroborates the higher Ti content of Ti_2Nb_8 films. A spatial distribution of Nb and Ti in $TiNb_9$ and Ti_2Nb_8 films annealed at 1000 °C, obtained from EDS mapping, is used to illustrate this in Fig. 8. Notably, the distribution of the elements confirms that the films are homogeneous.

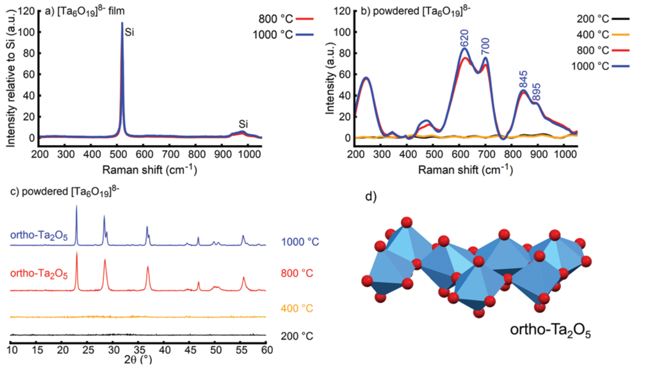

Fig. 6 Raman spectra of $[Ta_6O_{19}]^{8-}$ films annealed at 800 °C and 1000 °C, (b) Raman spectra and (c) PXRD patterns of powdered $[Ta_6O_{19}]^{8-}$ annealed at selected temperatures and (d) the *ortho*-Ta_2O_5 polymorph of Ta_2O_5. Red spheres represent oxygen atoms and dark blue polyhedra represent tantalum atoms. See ESI (Fig. S2-5†) for Raman signals of powdered $[Ta_6O_{19}]^{8-}$ annealed at 200–400 °C.

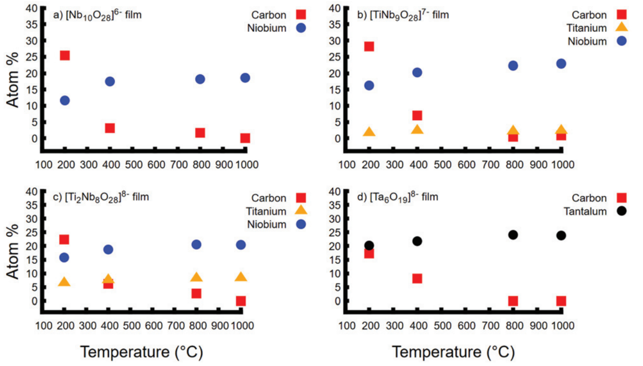

Fig. 7 Atomic composition of annealed Nb_{10} (a), $TiNb_9$ (b), Ti_2Nb_8 (c), and Ta_6 (d) films. See ESI (Table S5-1†) for details of full atomic composition. The carbon content decreases with annealing temperature in all cases.

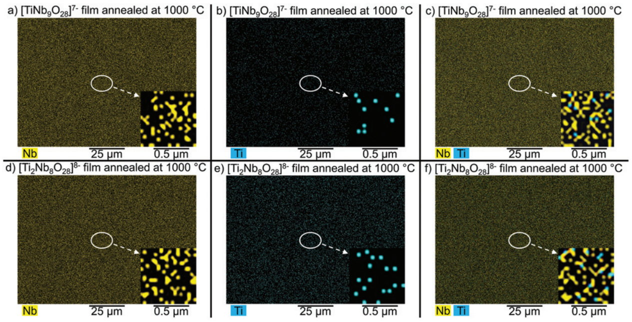

Fig. 8 EDS map of the spatial distribution of Nb (a), Ti (b) and Nb/Ti (c) in $TiNb_9$, and Nb (d), Ti (e) and Nb/Ti (f) in Ti_2Nb_8 films annealed at 1000 °C.

Multiple depositions of films

We also investigated repeated deposition of layers of polyoxometalates. Nb_{10} was deposited on silicon wafers that had been prepared by plasma treatment, and then annealed. At 800 °C, the film after a single deposition consisted of *ortho*-Nb_2O_5, had a thickness of 147 ± 5 nm according to ellipsometry. This film was again treated by ambient pressure plasma, and a new layer of Nb_{10} was spin-coated onto the first one. Pre-treatment of the film by plasma was necessary to ensure good adhesion between the layers. This process of repeated spin-coating and plasma treatment was repeated to deposit four successive layers of film, and we did this with all five polyoxometalates included in this study. After four layers of Nb_{10} had been spin-coated onto the silicon wafer, a final thickness of 235 ± 5 nm, as determined by SEM, was obtained when annealing at 800 °C (Fig. 9a). Notably, SEM showed that the film possessed voids with no obvious layering, and the films were determined to be smooth (roughness of ±24 nm) *via* AFM.

In contrast, when successive deposition was carried out with annealing at 1000 °C, a film of mono-Nb_2O_5 with a total thickness of 642 ± 46 nm was obtained (Fig. 9b). Here, two layers were observed, with a lower layer of thickness 199 ± 6 nm, and an upper layer with thickness 442 ± 44 nm. Voids were also apparent, but only in the upper layer and it had a roughness of ±55 nm. The presence of a distinct first layer in the mono-Nb_2O_5 film is indicative of successive layered deposition and subsequent stacking of the mono-Nb_2O_5 film. Though stacking of layers is not discernible for the *ortho*-Nb_2O_5 film, the larger thickness of this film (235 ± 5 nm), compared to the first layer of the *ortho*-Nb_2O_5 film (147 ± 5 nm), may be due to coalescence of the successively deposited layers of the *ortho*-Nb_2O_5 film. The increase in roughness as the films were annealed at 1000 °C is attributable to enhanced grain growth at higher temperatures, which occurs simultaneously with the phase change.

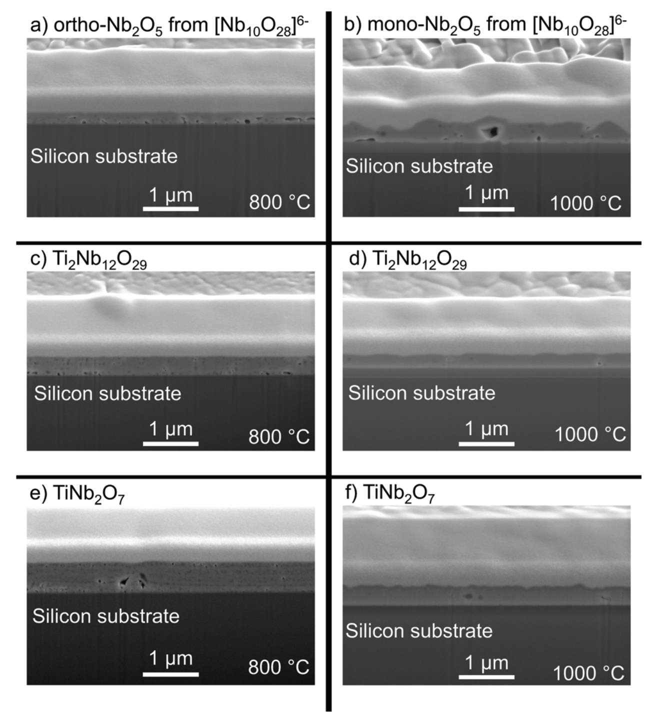

Fig. 9 Cross-section images for annealing: Nb_{10} at 800 °C (a) and 1000 °C (b); $TiNb_9$ at 800 °C (c) and 1000 (d); Ti_2Nb_8 at 800 °C (e) and 1000 (f) films after multiple depositions. Films annealed at 800 °C showed no layering, while the films annealed at 1000 °C exhibited two layers above the silicon substrate.

Layering of $TiNb_9$ and Ti_2Nb_8 films was also studied (Fig. 9c–f) and the thickness and roughness are summarised in Table S4-1.† After four successive depositions of $TiNb_9$ and Ti_2Nb_8 followed by annealing at 800 °C, $Ti_2Nb_{12}O_{29}$ and $TiNb_2O_7$ films were obtained, respectively, with no discernible layering, as with Nb_{10}. Furthermore, as with Nb_{10}, two layers were obtained at 1000 °C for both titanium–niobium oxide films and roughness increased for $Ti_2Nb_{12}O_{29}$ (±35.3 nm) but not $TiNb_2O_7$ (±13.8 nm). For both $Ti_2Nb_{12}O_{29}$ and $TiNb_2O_7$ films annealed at 1000 °C, the lower layers of the films were homogeneous and free of voids, while the voids were apparent only in the upper layer, like with Nb_{10}.

Successive deposition of four layers of Nb_6 and Ta_6 films annealed at 800 °C also yielded *ortho*-Nb_2O_5 and *ortho*-Ta_2O_5 films, respectively, which did not exhibit layering. The *ortho*-Nb_2O_5 film had voids (Fig. 10a) while the *ortho*-Ta_2O_5 film was homogeneous throughout (Fig. 10b). Furthermore, the Nb_6 film annealed at 1000 °C produced a layered mono-Nb_2O_5 film – similarly to Nb_{10} – with both layers of film being homogeneous. The Ta_6 film annealed at 1000 °C also formed a layered *ortho*-Ta_2O_5 film that was smooth and free of voids in both layers. The tendency for Ta_6 to form smooth, homogeneous Ta_2O_5 films is likely a consequence of its tendency to gel, instead of crystallising like Nb_6, as observed with the removal of water during rotary evaporation.[27]

The *ortho*-Nb_2O_5 film possessed more voids than the mono-Nb_2O_5 film, when comparing the *ortho*-Nb_2O_5 film as a whole

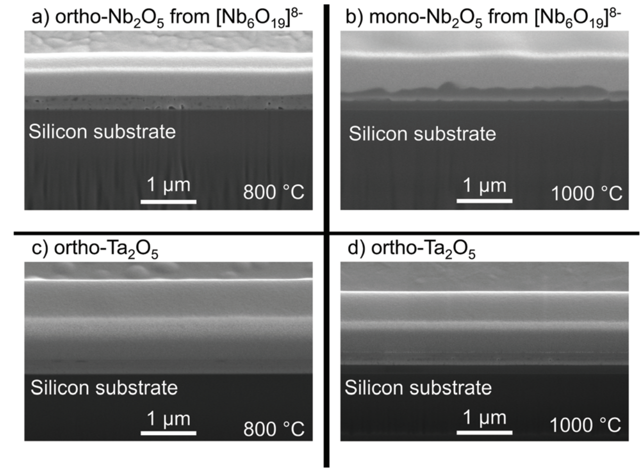

Fig. 10 Cross-section images for annealing: Nb_6 at 800 °C (a) and 1000 °C (b); Ta_6 at 800 °C (c) and 1000 °C (d). The tantalate films are noticeably smoother and more homogeneous than the niobate films.

to the lower layer of the mono-Nb_2O_5 film. In the solid state, Si–O–Nb bond formation is encouraged at the silica–Nb_2O_5 interface at higher temperatures.[62,63] Therefore, more Si–O–Nb bonds will form when annealing the Nb_2O_5 film at 1000 °C, compared to 800 °C. This contributes to film densification at higher temperatures. The homogeneity of the lower layer of mono-Nb_2O_5 film in contrast to the presence of voids in the *ortho*-Nb_2O_5 film and in the upper layer of the mono-Nb_2O_5 film, is thus likely due to poor densification of the latter.

The formation of a distinct first layer in $Ti_2Nb_{12}O_{29}$ and $TiNb_2O_7$ is similarly likely dependent on Si–O–Nb bond formation. However, Si–O–Ti bonds are considered to contribute to the binding of the film to the substrate as complete incorporation of Ti into the silica network occurs at high temperatures (1000 °C).[64] The prevalence of this bonding is inherently lower than that of the Si–O–Nb bonds, based on the partial occupancy of Ti atoms within the crystal lattice of $Ti_2Nb_{12}O_{29}$ and $TiNb_2O_7$.[41,42] The presence of the Ti atoms within the crystal lattice contributes to formation of Nb–O–Ti bonds, which also facilitate the adhesion of subsequent layers of the titanium–niobium oxides and supports film densification. Hence, the upper layers of the $Ti_2Nb_{12}O_{29}$ and $TiNb_2O_7$ films annealed at 1000 °C possessed fewer voids than the analogous layer of mono-Nb_2O_5 film.

Conclusions

The controlled deposition of metal oxide thin films is possible *via* an iterative spin-coating and annealing process of POMs. This approach allows deposition of alkali-free, crystalline metal oxide thin films with tuneable thickness and roughness. Notably, the optical and energy storage properties of metal oxide films is dependent on their crystal structures. The TMA salts of Nb_6, Ta_6, Nb_{10}, $TiNb_9$ and Ti_2Nb_8 clusters allow the deposition of orthorhombic and monoclinic Nb_2O_5, Ta_2O_5, $Ti_2Nb_{12}O_{29}$ and $TiNb_2O_7$ from aqueous solutions, depending on precursor and conditions. The substitution of a combustible organic counter cation, here tetramethylammonium, for the more common alkali–metal counter ions not only allows for the deposition of alkali-free metal oxide films, but also allows for increased flexibility in the tuning of the composition and properties of the films. Furthermore, the ability to deposit films with tuneable crystallinity is crucial to developing high quality, pristine metal oxide thin films for advancing nanotechnology and semiconductor development. We also showed that Raman spectroscopy is a powerful and convenient method of determining the phase purity of niobium pentoxide (orthorhombic or monoclinic).

The inclusion of heterometal atoms in polyoxometalates leads to different solid-state structures, even when the difference in substitution is limited to a single atom. The site-specific inclusion of Ti within the decametalate structure is exemplary of this and it can be inferred that the site-specific inclusion of other heterometals may elicit a similar effect. There is thus great potential for developing this technique to include other types of heterometals, such as those that have been shown to be catalytically active in different reactions. By including these in a chemically inert substrate such as niobium pentoxide, chemical processes may be adapted to take place in environments that would otherwise be too demanding.

Conflicts of interest

There are no conflicts to declare.

Acknowledgements

C. A. O thanks the Kempe Foundation (JCK-2029.1) and the Swedish Research Council (2018-07039) for generous support. M. A. R thanks the Department of Chemistry at Umeå University for a postgraduate fellowship. Prof. William H. Casey at UC Davis and Dr Sven Albrecht from TANIOBIS GmbH, are equally thanked for generous gifts of hydrous Nb_2O_5 and hydrous Ta_2O_5, respectively. We also thank Prof. Markus Broström for providing a furnace for annealing experiments, and Drs Hussein Kanbar and Cheng Choo Lee (Umeå Core Facility of Electron Microscopy) for assisting with PXRD and FIB-SEM/EDS measurements, respectively. Support towards the Vibrational Spectroscopy Core Facility by the Chemical Biological Centre and the Department of Chemistry at Umeå University is greatly acknowledged.

References

1 Y. Pozdeev, *Qual. Reliab. Eng. Int.*, 1998, **14**, 79–82.
2 D. Pradhan, A. W. Wren, S. T. Misture and N. P. Mellott, *Mater. Sci. Eng., C*, 2016, **58**, 918–926.
3 N. Wang, H. Li, J. Wang, S. Chen, Y. Ma and Z. Zhang, *ACS Appl. Mater. Interfaces*, 2012, **4**, 4516–4523.
4 J. Ge, F. Wang, Z. Xu, X. Shen, C. Gao, D. Wang, G. Hu, J. Gu, T. Tang and J. Wei, *J. Mater. Chem. B*, 2020, **8**, 2618–2626.
5 Y. Guo, K. Xie, W. Jiang, L. Wang, G. Li, S. Zhao, W. Wu and Y. Hao, *ACS Biomater. Sci. Eng.*, 2019, **5**, 1123–1133.
6 Q. Zhao, R. O. Behunin, P. T. Rakich, N. Chauhan, A. Isichenko, J. Wang, C. Hoyt, C. Fertig, M. h. Lin and D. J. Blumenthal, *APL Photonics*, 2020, **5**(116103), 1–8.
7 N. Maruthi, M. Faisal, N. Raghavendra, B. P. Prasanna, S. R. Manohara and M. Revanasiddappa, *Synth. Met.*, 2021, **275**(116744), 1–9.
8 M. Dinu, L. Braic, S. C. Padmanabhan, M. A. Morris, I. Titorencu, V. Pruna, A. Parau, N. Romanchikova, L. F. Petrik and A. Vladescu, *J. Mech. Behav. Biomed. Mater.*, 2020, **103**, 103582.
9 Y. Ge, Y. Wang, J. Chen, Y. Zou, L. Guo, J. Ouyang, D. Jia and Y. Zhou, *J. Alloys Compd.*, 2018, **767**, 7–15.
10 W. Hu, J. Xu, X. Lu, D. Hu, H. Tao, P. Munroe and Z.-H. Xie, *Appl. Surf. Sci.*, 2016, **368**, 177–190.

11 J. Xu, X. k. Bao, T. Fu, Y. Lyu, P. Munroe and Z.-H. Xie, *Ceram. Int.*, 2018, **44**, 4660–4675.

12 J. W. Mantz, *Global Studies Review*, 2008, **4**, 12–14.

13 T. Ibn-Mohammed, S. C. L. Koh, I. M. Reaney, A. Acquaye, D. Wang, S. Taylor and A. Genovese, *Energy Environ. Sci.*, 2016, **9**, 3495–3520.

14 D. Fast, M. Clark, L. Fullmer, K. Grove, M. Nyman, B. Gibbons and M. Dolgos, *Thin Solid Films*, 2020, **710**(138270), 1–6.

15 M. Nyman, L. J. Criscenti, F. Bonhomme, M. A. Rodriguez and R. T. Cygan, *J. Solid State Chem.*, 2003, **176**, 111–119.

16 M. Nyman, *Dalton Trans.*, 2011, **40**, 8049–8058.

17 L. Zhang and Z. Chen, *Int. J. Energy Res.*, 2020, **44**, 3316–3346.

18 H.-Y. Zhao, Y.-Z. Li, J.-W. Zhao, L. Wang and G.-Y. Yang, *Coord. Chem. Rev.*, 2021, **443**(213966), 1–23.

19 M. Amiri, N. P. Martin, C. L. Feng, J. K. Lovio and M. Nyman, *Angew. Chem., Int. Ed.*, 2021, **60**, 12461–12466.

20 N. P. Martin and M. Nyman, *Angew. Chem., Int. Ed.*, 2021, **60**, 954–960.

21 N. P. Martin, E. Petrus, M. Segado, A. Arteaga, L. N. Zakharov, C. Bo and M. Nyman, *Chem. – Eur. J.*, 2019, **25**, 10580–10584.

22 C. A. Ohlin, E. M. Villa, J. C. Fettinger and W. H. Casey, *Angew. Chem., Int. Ed.*, 2008, **47**, 5634–5636.

23 C. A. Ohlin, E. M. Villa, J. C. Fettinger and W. H. Casey, *Dalton Trans.*, 2009, 2677–2678, DOI: 10.1039/B900465C.

24 J.-H. Son and W. H. Casey, *Chem. – Eur. J.*, 2016, **22**, 14155–14157.

25 J.-H. Son, J. Wang and W. H. Casey, *Dalton Trans.*, 2014, **43**, 17928–17933.

26 M. A. Rambaran, M. Pascual-Borràs and C. A. Ohlin, *Eur. J. Inorg. Chem.*, 2019, 3913–3918, DOI: 10.1002/ejic.201900750.

27 L. B. Fullmer, R. H. Mansergh, L. N. Zakharov, D. A. Keszler and M. Nyman, *Cryst. Growth Des.*, 2015, **15**, 3885–3892.

28 R. H. Mansergh, L. B. Fullmer, D.-H. Park, M. Nyman and D. A. Keszler, *Chem. Mater.*, 2016, **28**, 1553–1558.

29 P. Amaravathy, S. Sowndarya, S. Sathyanarayanan and N. Rajendran, *Surf. Coat. Technol.*, 2014, **244**, 131–141.

30 V. K. Balla, S. Banerjee, S. Bose and A. Bandyopadhyay, *Acta Biomater.*, 2010, **6**, 2329–2334.

31 V. K. Balla, S. Bodhak, S. Bose and A. Bandyopadhyay, *Acta Biomater.*, 2010, **6**, 3349–3359.

32 M. Grobelny, M. Kalisz, M. Mazur, D. Wojcieszak, D. Kaczmarek, J. Domaradzki, M. Świniarski and P. Mazur, *Thin Solid Films*, 2016, **616**, 64–72.

33 E. I. Ko and J. G. Weissman, *Catal. Today*, 1990, **8**, 27–36.

34 R. A. Rani, A. S. Zoolfakar, A. P. O'Mullane, M. W. Austin and K. Kalantar-Zadeh, *J. Mater. Chem. A*, 2014, **2**, 15683–15703.

35 H. Schäfer, R. Gruehn and F. Schulte, *Angew. Chem., Int Ed Engl.*, 1966, **5**, 40–52.

36 S. Lagergren and A. Magnéli, *Acta Chem. Scand., Ser. A*, 1952, **6**, 444–446.

37 N. C. Stephenson and R. S. Roth, *Acta Crystallogr., Sect. B: Struct. Sci.*, 1971, **27**, 1037–1044.

38 N. C. Stephenson and R. S. Roth, *J. Solid State Chem.*, 1971, **3**, 145–153.

39 I. P. Zibrov, V. P. Filonenko, M. Sundberg and P.-E. Werner, *Acta Crystallogr., Sect. B: Struct. Sci.*, 2000, **56**, 659–665.

40 C. A. Ohlin, E. M. Villa and W. H. Casey, *Inorg. Chim. Acta*, 2009, **362**, 1391–1392.

41 A. D. Wadsley, *Acta Crystallogr.*, 1961, **14**, 664–670.

42 A. D. Wadsley, *Acta Crystallogr.*, 1961, **14**, 660–664.

43 R. B. V. Dreele, A. K. Cheetham and J. S. Anderson, *Proc. R. Soc. London, Ser. A*, 1974, **338**, 311–326.

44 X. Wu, J. Miao, W. Han, Y.-S. Hu, D. Chen, J.-S. Lee, J. Kim and L. Chen, *Electrochem. Commun.*, 2012, **25**, 39–42.

45 N. G. Eror and U. Balachandran, *J. Solid State Chem.*, 1982, **45**, 276–279.

46 S. Deng, Z. Luo, Y. Liu, X. Lou, C. Lin, C. Yang, H. Zhao, P. Zheng, Z. Sun, J. Li, N. Wang and H. Wu, *J. Power Sources*, 2017, **362**, 250–257.

47 S. Lou, X. Cheng, J. Gao, Q. Li, L. Wang, Y. Cao, Y. Ma, P. Zuo, Y. Gao, C. Du, H. Huo and G. Yin, *Energy Storage Mater.*, 2018, **11**, 57–66.

48 K. J. Griffith, Y. Harada, S. Egusa, R. M. Ribas, R. S. Monteiro, R. B. Von Dreele, A. K. Cheetham, R. J. Cava, C. P. Grey and J. B. Goodenough, *Chem. Mater.*, 2020, **33**, 4–18.

49 Y. Yang and J. Zhao, *Adv. Sci.*, 2021, **8**(2004855), 1–24.

50 D. Pham-Cong, J. Kim, V. T. Tran, S. J. Kim, S.-Y. Jeong, J.-H. Choi and C. R. Cho, *Electrochim. Acta*, 2017, **236**, 451–459.

51 C. Yang, S. Yu, Y. Ma, C. Lin, Z. Xu, H. Zhao, S. Wu, P. Zheng, Z.-Z. Zhu, J. Li and N. Wang, *J. Power Sources*, 2017, **360**, 470–479.

52 A. Llordés, G. Garcia, J. Gazquez and D. J. Milliron, *Nature*, 2013, **500**, 323–326.

53 A. Llordés, A. T. Hammack, R. Buonsanti, R. Tangirala, S. Aloni, B. A. Helms and D. J. Milliron, *J. Mater. Chem.*, 2011, **21**, 11631–11638.

54 A. Llordés, Y. Wang, A. Fernandez-Martinez, P. Xiao, T. Lee, A. Poulain, O. Zandi, C. A. Saez Cabezas, G. Henkelman and D. J. Milliron, *Nat. Mater.*, 2016, **15**, 1267–1273.

55 C. A. Saez Cabezas, K. Miller, S. Heo, A. Dolocan, G. LeBlanc and D. J. Milliron, *Chem. Mater.*, 2020, **32**, 4600–4608.

56 H. Chaudhary, I. A. Iashchishyn, N. V. Romanova, M. A. Rambaran, G. Musteikyte, V. Smirnovas, M. Holmboe, C. A. Ohlin, Z. M. Svedruzic and L. A. Morozova-Roche, *ACS Appl. Mater. Interfaces*, 2021, **13**, 26721–26734.

57 E. M. Villa, C. A. Ohlin, E. Balogh, T. M. Anderson, M. D. Nyman and W. H. Casey, *Angew. Chem., Int. Ed.*, 2008, **47**, 4844–4846.

58 E. M. Villa, C. A. Ohlin, E. Balogh, T. M. Anderson, M. D. Nyman and W. H. Casey, *Am. J. Sci.*, 2008, **308**, 942–953.

59 E. M. Villa, C. A. Ohlin and W. H. Casey, *J. Am. Chem. Soc.*, 2010, **132**, 5264–5272.

60 E. M. Villa, C. A. Ohlin, J. R. Rustad and W. H. Casey, *J. Am. Chem. Soc.*, 2009, **131**, 16488–16492.

61 J. M. Jehng and I. E. Wachs, *Chem. Mater.*, 1991, **3**, 100–107.

62 M. S. P. Francisco and Y. Gushikem, *J. Mater. Chem.*, 2002, **12**, 2552–2558.

63 S. Morselli, P. Moggi, D. Cauzzi and G. Predieri, in *Stud. Surf. Sci. Cat*, ed. B. Delmon, P. A. Jacobs, R. Maggi, J. A. Martens, P. Grange and G. Poncelet, Elsevier, 1998, vol. 118, pp. 763–772.

64 C. C. Perry, X. Li and D. N. Waters, *Spectrochim. Acta, Part A*, 1991, **47**, 1487–1494.